

Towards Quality Advancement of Underwater Machine Vision with Generative Adversarial Networks

Xingyu Chen, Junzhi Yu, *Senior Member, IEEE*, Shihan Kong, Zhengxing Wu, Xi Fang, and Li Wen

Abstract—Underwater machine vision attracts more attention, but the terrible quality prohibits it from a wide range of applications. There exist many algorithms to solve this problem, but the real-time and adaptive method is frequently deficient. In this paper, based on filtering and Generative Adversarial Networks (GANs), two approaches are proposed for the aforementioned issue, i.e., a filtering-based restoration scheme (FRS) and a GAN-based restoration scheme (GAN-RS). Distinct from the previous methods, FRS restores underwater image in the frequency domain, which is composed of parameter search, filtering, and enhancement. Aiming to further improve the image quality, the GAN-RS is able to adaptively restore underwater machine vision in real time without any pretreatment. In particular, the information in Lab color space and the dark channel is developed as the loss function, namely underwater index loss and dark channel prior loss. More specifically, learning from the underwater index, the discriminator is equipped with a carefully crafted underwater branch to predict the underwater probability of an image. Multi-stage loss strategy, then, is developed to guarantee the effective training of GANs. Through extensive comparisons on image quality and applications, the superiority of the proposed approaches is confirmed. As a result, the GAN-RS is much faster and achieves the state-of-the-art performance on color correction, contrast stretch, dehazing, and feature restoration of various underwater scenes. Note that the source code will be made available.

Index Terms—Underwater vision, image processing, Generative Adversarial Networks (GANs), image restoration.

I. INTRODUCTION

Ocean science has been vigorously studied in recent years, in which underwater vision has received considerable attention due to the visual information is visibly richer than traditional measurements, like sonar [1] and laser system [2]. Thereby, a multitude of underwater vision tasks emerge. For instance, to overcome the problem with the low contrast underwater vision, Chuang *et al.* utilized a segmentation algorithm for multiple fish-tracking [3]; Lee *et al.* proposed a color

This work was supported by the National Natural Science Foundation of China (nos. 61633004, 61633020, 61603388, and 61633017), and by the Beijing Natural Science Foundation (nos. 4164103 and 4161002).

X. Chen and S. Kong are with the University of Chinese Academy of Sciences, Beijing 100049, China, {chenxingyu2015, kongshihan2016}@ia.ac.cn

X. Chen, J. Yu, S. Kong, and Z. Wu are with the State Key Laboratory of Management and Control for Complex Systems, Institute of Automation, Chinese Academy of Sciences, Beijing 100190, China, {chenxingyu2015, junzhi.yu, kongshihan2016, zhengxing.wu}@ia.ac.cn

X. Fang and L. Wen are with the School of Mechanical Engineering and Automation, Beihang University, Beijing 100191, China, {fangxi, liwen}@buaa.edu.cn

restoration algorithm to achieve high-performance underwater object detection [4]. Apparently, all underwater visual tasks can benefit from high-quality underwater images or videos, but underwater scenes are far more terrible and changeable than terrestrial environments. Thus, the advancement of underwater machine vision has become a research hotspot.

Color distortion, contrast reduction, and haziness are typical issues of image degeneration. In recent decades, many approaches to restoration have been proposed. Gray World (GW) algorithm correct color with the assumption that the averages of RGB components in a white-balanced image tend to be the same gray value [5]. As a classical alternative to contrast stretch, histogram equalization has been developed maturely, e.g., contrast limited adaptive histogram equalization (CLAHE) [7]. In terms of dehazing, He *et al.* created the dark channel prior (DCP) algorithm for haze removal [9]. The aforementioned methods solve the problem with degeneration in a particular perspective, but underwater vision degeneration contains all the three aspects. Thus, some works for underwater image restoration are conducted based on information estimation. For example, Chiang *et al.* analyzed the wavelength of underwater light then compensated it to achieve a superior color fidelity [6]. However, underwater scenes are changeable, and the existing literature is hard to handle a variety of underwater vision degeneration with a constant model or parameters. Moreover, few studies emphasize the time efficiency, which is a pivotal factor for autonomous maritime and underwater operations. Thereby, it is essential to develop a real-time and adaptive method for underwater vision restoration.

Recently, Generative Adversarial Networks (GANs) [18] is successfully employed in image-to-image translation tasks, e.g., style transfer and super-resolution [23]. The GANs is a minimax two-player game between the generator G and the discriminator D . Via an adversarial training process, the discriminator D learns to distinguish the real image and the synthesized one, and the generator learns to fool the discriminator. When D can hardly distinguish the real and the synthesized sample, what generated by G is closely similar to the real one. It is obvious that the image restoration can be treated as the image-to-image translation, so we ensure that the GANs is able to restore the underwater scenes, if trained with the original underwater images and the corresponding in-air versions. More specifically, an original underwater image serves as the input, then G provides its production. If D can hardly distinguish the synthesized data and the in-air version,

the generator restores the underwater image successfully. Furthermore, taking advantage of the powerful fitting capacity in the neural networks, the GANs-based method is able to work adaptively. Unfortunately, in-air versions of underwater environments are almost impossible to be obtained. As a compromise solution, the synthetic in-air data based on a traditional restoration method can be utilized. By this means, the GANs yet can hardly perform better than the employed restoration method as a result. Therefore, improvements need to be involved in the existing GANs framework in order to break through the limitation.

In this paper, for the purpose of adaptively advancing the underwater machine vision in real time, we propose a filtering-based restoration scheme (FRS) and a GANs-based restoration scheme (GAN-RS). At first, we introduce underwater degeneration problem into the frequency domain, and develop the FRS with artificial fish school algorithm, Wiener Filter, and CLAHE. Instead of the traditional information of underwater image formation, the high-level parameters are designed to avoid frame-by-frame information estimation or search in similar environments. Then, the results of the FRS are employed to train a supervised GANs, and the GAN-RS is built to improve the quality of underwater machine vision further. Creatively, the DCP loss and underwater index loss are designed for training, and the combination of loss functions obeys the multi-stage loss strategy. Correspondingly, an underwater branch is added to the discriminator, which predicts the probability that an image is aquatic or not. Extensive comparison experiments verify the restoration quality, time efficiency, and adaptability of the proposed algorithms. According to the best knowledge of the authors, few restoration methods in existing literature have capability of realtimeness and adaptability. The contributions made in this paper are summarized as follows:

- As a traditional method, the FRS requires less message from an image. Hence, the FRS is well suited to be used in real-time applications.
- The underwater index loss and underwater branch guarantee the GAN-RS to obtain a better comprehension of underwater attributes, and make further improvements on restoration quality. Moreover, the GAN-RS no longer needs any information estimation or parameter search.
- The GAN-RS is extremely fast, and achieves the state-of-the-art restoration performance. Further, the GAN-RS can be leveraged as a general framework to enhance or combine any other restoration methods for clear vision, time efficiency, and adaptability.

The remainder of the paper is organized as follows. The underwater image restoration and image-to-image translation is reviewed in Section II. The FRS and its components are detailed in Section III. Section IV analyzes the GAN-RS, followed by its architecture and training details. Experimental results and analyses are provided in Section V. Finally, concluding remarks are offered in Section VI.

II. RELATED WORK

A. Formation of Underwater Vision

A general analysis of underwater vision was presented in [11]. Schechner and Karpel modeled the transmission of underwater optical signal, which was composed of the direct transmission and the forward scattering. A part of optical energy will be absorbed during the direct transmission, causing color distortion and low contrast. The signal of direct transmission D was expressed as exponential decay:

$$d = e^{-\eta z} j \quad (1)$$

where η is the attenuation coefficient; z is the object-to-camera distance; and j is the signal from the object.

In addition, the forward scattering leads image to be hazy. Therefore, the signal after forward scattering F could be formulated by convolution:

$$f = d * g_z \quad (2)$$

where g_z is a point spread function [12].

On the other hand, Schechner and Karpel also introduced the backscattered light b , which is from ambient illumination source and scattered into the line of sight. Thus, the degenerated signal l is the comprehensive result of these three phenomena:

$$l = d + f + b. \quad (3)$$

B. Traditional Underwater Image Restoration Methods

1) *Estimation-Based Restoration Method*: A group of existing methods for restoring underwater image are based on image formation model (IFM). Peng and Cosman made a comprehensive summary on image information estimation based on DCP or MIP (maximum intensity prior), and the restoration method based on image blurriness and light absorption (RBLA) was proposed [14]. Consistent with [11], the IFM can be simplified as:

$$l_\lambda(x) = j_\lambda(x)t_\lambda(x) + B_\lambda(1 - t_\lambda(x)), \quad \lambda \in r, g, b \quad (4)$$

where l_λ is the degenerated signal; j_λ is the original object radiance; B_λ is the background light (BL); and t_λ represents transmission map (TM), denoting the percentage of the object radiance received by camera. Obviously, B_λ and t_λ are hard to be measured, so they need to be estimated. Classically, DCP is frequently-used tool for estimation of BL and TM, which is defined as follows:

$$l_{dark}^{rgb} = \min_{p \in \Omega(P)} \{ \min_{\lambda \in \{r, g, b\}} l_\lambda(p) \} \quad (5)$$

where p represent the pixel coordinate, and Ω is a image patch around a pixel P .

According to [9], the BL is determined as the top 0.1% brightest pixels in l_{dark}^{rgb} , and t_λ also can be estimated with the assumption of $j_{dark}^{rgb} = 0$.

Based on the aforementioned theory, Li *et al.* hierarchically estimated the BL by quad-tree subdivision, avoidance of suspended particles, and bright disturbance removal [10]. Finally, the pixels with the maximum blue-red difference in the original image was selected as the global BL. Meanwhile, the method

for TM estimation was characterized by minimum information loss, which was defined in a local block for red channel. Then, smoothed with the relative total variation [16], the TM can be treated as the linear combination of the red channel blocks.

As an effective tool for nonlinear fitting, neural network has been recently utilized for the IFM estimation. Shin *et al.* proposed a CNNs architecture to estimate the BL and the TM synchronously, consisting of multi-scale fusion, multi-scale feature extraction, and nonlinear regression [17].

Therefore, the original object radiance j_λ can be recovered by (4) after the BL and TM are obtained. More variants of estimation-based method are discussed in [14].

2) *Fusion-Based Restoration Method*: Depending on multi-map weighted fusion, another group of restoration is model-free [8]. Ignoring IFM, the approach proposed by Ancuti *et al.* derived the inputs and the weights from the degraded image. There were two input maps, i.e., the white balanced version and the noise-reduced version. The former could be obtained by a simple illumination estimation while the latter was processed by temporal bilateral filter [15], which performed well on edges and temporal coherence preservation.

Additionally, weight maps of the fusion were designed, including Laplacian contrast weight (WL), local contrast weight (WLC), saliency weight (WS), and exposedness weight (WE). According to the authors' description, WL dealt with global contrast; WLC comprised the relation between each pixel and its neighborhoods average; WS emphasized the discriminating objects that lose their prominence in the underwater scene; and WE also preserved a constant appearance of the local contrast.

Despite no IFM in the fusion-based framework, a large body of messages from a specific image are still demanded. Unlike the traditional methods, this paper restores underwater machine vision from another perspective. Our algorithms ignore any low-level information, i.e., BL and TM, in a degenerated image, the frame-by-frame estimation of which is time-consuming. For example, the average processing time of the dehazing and the contrast enhancement algorithms in [10] are 0.764 s and 0.968 s, which stand out among the analogous methods. Instead, two high-level parameters would be searched in FRS, which can be shared with similar scenes. Move a step further, parameter search is also omitted in the GAN-RS, and thus, the proposed methods perform better on the realtimeness and adaptability for changeable underwater environments.

C. GANs-Based Image-to-Image Translation

With the development of deep learning, especially GANs, approaches to image-to-image translation has been developed rapidly in recent years. In general, the learning-based methods can be divided into two categories, i.e., supervised and unsupervised image-to-image translation.

1) *Supervised Approaches*: If there is ground truth, the network can be trained in the supervised way [22]–[26]. Zhu *et al.* used GANs to learn the manifold of natural images, and the generator presented the scenes or objects from the profiles [22]. For style transfer and super-resolution, Johnson *et al.* proposed a perceptual loss function with the VGG-16

network [23], [31]. Further, combining the adversarial loss with the mean squared error (MSE) and VGGNet, Ledig *et al.* reconstructed a perceptual loss to guide G more effectively. As a result, a fourfold increase in resolution was achieved [24]. Meanwhile, residual blocks were employed to design the generative network [32]. Isola *et al.* proposed a general framework to image-to-image translation problems based on conditional GANs (cGANs), namely pix2pix [19], [25]. To share the low-level information with deconvolution layers, U-Net with skip connections was used as the generator [30]. On the other hand, following [21], the idea of PatchGAN was utilized to build a fully-convolutional discriminator. Wang *et al.* also attempted to build a generic framework to learn the relationship from paired images. Their method Perceptual Adversarial Networks (PAN) was also equipped with a perceptual adversarial loss based on the hidden layers of the discriminative network and the skip-connection generator [26]. The latter two frameworks succeed in various tasks, including labels to street scene, labels to facade, aerial photo to map, day to night, edges to photo, rain to de-rain, and corrupted to inpainted.

2) *Unsupervised Approaches*: In some cases, the ground truth is hard to be obtained. Some unsupervised methods are developed to overcome this difficulty [27]–[29]. For lack of labeled data, Dong *et al.* designed an unsupervised framework with three stages of learning shared feature, learning image encoder, and translation. This method succeeded in gender transformation and face swapping [27]. Extending from pix2pix, Zhu *et al.* proposed a general unsupervised framework, namely CycleGAN [28], whose main idea was the minimization of reconstruction error between two sets of training data. Correspondingly, two group of GANs were employed to realize bidirectional translation. That is, G_1 mapped data distribution of set-I into that of set-II while G_2 performed a vice mapping, and two discriminators guided respective generators with cycle consistency loss. CycleGAN worked well in the same tasks of pix2pix in the unsupervised way, but its performance was not comparable to that of pix2pix.

There are also some semi-supervised approaches to image-to-image translation, like [33]. However, supervised methods are more suitable to be employed for underwater restoration, which demands precise translation. Distinct from aforementioned literature, the supervision in GAN-RS is twofold. That is, despite the paired training data, the target image serves as a guidance rather than the output from a desirable generator. Meanwhile, the discriminator should learn to distinguish not only the real and generated data, but also whether a scene is underwater or not, while the generative model should find a compromise.

D. Underwater Application of GANs

The nearest work to this paper are [34] and [35]. Since it was hard to obtain the in-air ground truth for an underwater scene, Li *et al.*, on the contrary, collected image set with depth information in air, and use WaterGAN to convert it into a water-like version to obtain a large body of training data [34]. In the next step, this data in turn are used to train a network equipped with the depth estimation network and color

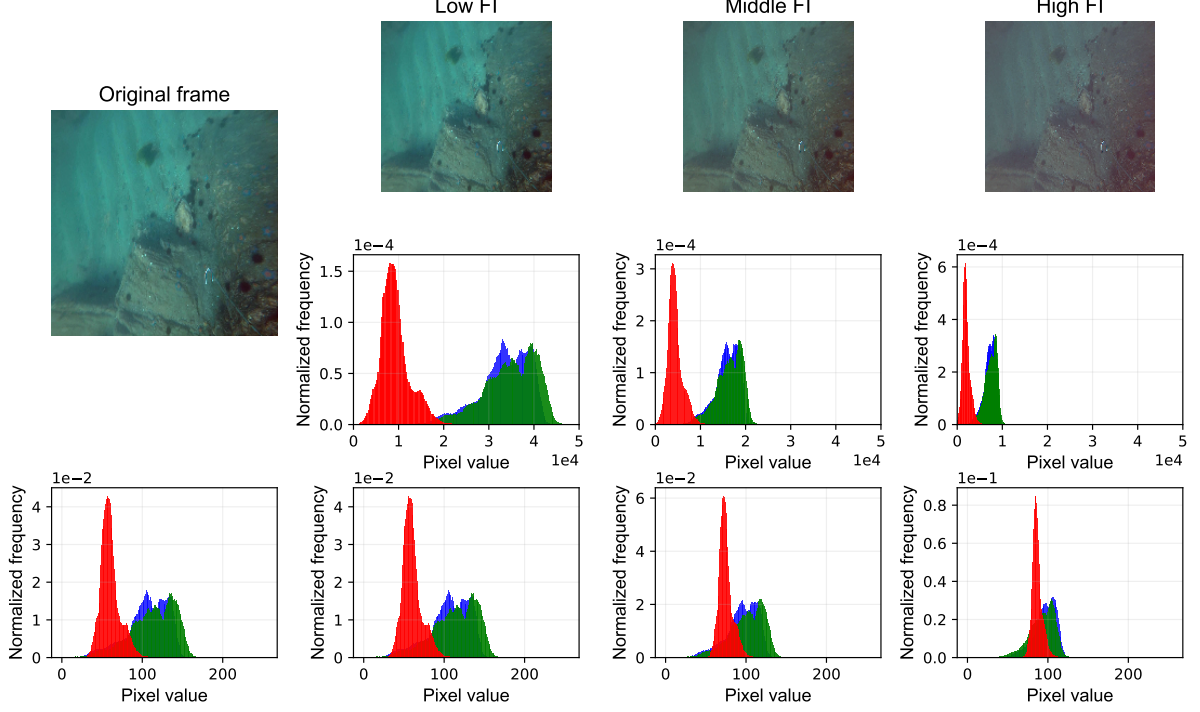


Fig. 1. Balance trend of RGB-channel with the increasing FI. The first column is original frame and its histogram, and the latter columns present the filtered version (the second line) and the normalized version (the third line).

correction network to achieve white balance for an underwater image. Inspired by cycle consistency [28], Li *et al.* proposed a weakly supervised color transfer method with GANs for color correction, and a loss function for structural similarity was developed to preserve the original content and structure [35].

Different from the previous application, our dataset for training is captured on the seabed rather than the synthetic data from in-air scene. The proposed filtering-based method helps them escape from underwater conditions roughly. Meanwhile, our supervised framework is able to save image content and structure better.

III. FILTERING-BASED RESTORATION SCHEME

Our previous work proposed a real-time and unsupervised advancement scheme for restoring underwater vision [36]. In this section, we will firstly introduce the filtering-based restoration scheme extended from [36], which is composed of pre-search, filtering, and post-enhancement. As an initial process, pre-search aims to find the optimal parameters for filtering. In the next step, Wiener Filter is employed to solve the underwater degeneration in frequency domain, and the color distortion and haziness will be settled. Given the enhancement methods have been developed, the CLAHE is directly utilized as the operation of post-enhancement to make up the contrast compression caused by filtering.

A. Filtering Method

1) *Core Theory and Operation:* In general, the degeneration of underwater vision is caused by absorption, forward scattering, and backward scattering. The wavelength λ , water

depth D , and the object-to-camera distance z are of importance in the IFM. With the IFM as the starting point, we treat this problem in a concise view, i.e., the color distortion is produced by absorption; the haziness is led by forward and backward scattering scattering, while the backward scattering also incurs the noise. Thus, the degeneration model is formulated as follows:

$$l_\lambda = m(h^{fs}(z), h^{bs}(D, z)) * e^{-\eta(\lambda, D)z} j_\lambda + n(D, z) \quad (6)$$

where $h^{fs}(z)$, $h^{bs}(D, z)$ stand for a hazing convolution template related to forward and backward scattering, respectively; $e^{-\eta(\lambda, D)z}$ is the absorption term; $n(D, z)$ denotes the noise introduced by backward scattering. In particular, owing to the consistent effect of $h^{fs}(z)$ and $h^{bs}(D, z)$, it is not essential to distinguish them, so they can be unified with $h(D, z)$:

$$l_\lambda = h(D, z) * e^{-\eta(\lambda, D)z} j_\lambda + n(D, z). \quad (7)$$

The dehazing, thereby, has been converted into a deconvolution task. In the next step, the convolution operation inspired us to the Fourier transform. Thus, the above analysis can be transferred to frequency domain:

$$L_\lambda = e^{-\eta(\lambda, D)z} \mathcal{H}_\lambda(D, z) * J_\lambda + \mathcal{N}(D, z) \quad (8)$$

where the symbol $.*$ denotes elements-wise multiply for a matrix.

The turbulence model proposed by Hufnagel and Stanley [37] is used to formulate \mathcal{H} :

$$\mathcal{H}(u, v) = e^{-k(u^2 + v^2)^{5/6}} \quad (9)$$

where u, v are frequency variables; k is associated with the intensity of turbulent media. Note that k wraps D, z , i.e., $k = k(D, z)$. Thus, serving as a high-level parameter, k plays a essential role for dehazing.

For deconvolution, Wiener Filter is employed, which is a classical structure for signal processing:

$$\hat{L}_\lambda(u, v) = \left[\frac{\mathcal{H}^c(u, v)}{|\mathcal{H}(u, v)|^2 + R} \right] J_\lambda(u, v) \quad (10)$$

where $R = R(D, z)$ is the reciprocal of signal to noise ratio, which is responsible for noise suppression.

The output of Wiener Filter has escaped from the forward and backward scattering ideally.

2) *Filtering-Based Color Correction*: In this sub-section, a fast and model-free color correction will be introduced, namely filtering-based color correction (FCC). In the meantime, the necessity of post-enhancement will be illustrated.

There is another significant effect on contrast caused by filtering, which can be used to correct the color distortion, and FCC gives a normalized version of the output signals from Wiener Filter. As shown in Fig. 1, the filtering compresses the distribution of pixel value in RGB-channel simultaneously, which leads to a narrower-shape histogram curves with an increasing filtering intensity (FI). Note that the ratio of the mean pixel value in RGB-channel is constant during the filtering. Furthermore, if the filtered signal is normalized, the distribution will become balanced, and the higher FI leads to a stronger balance trend.

However, with the balance of color, the contrast is compressed. As illustrated in Fig. 1, the histogram curves become narrower. To make up this phenomenon, the post-enhancement is deemed necessary to follow the operation of filtering. By this means, the proposed FRS generates a color-balanced and contrast-stretched underwater vision with appropriate filtering parameters, or k, R .

B. Pre-Search

In this section, we provide an improved artificial fish school algorithm (AFSA) [38] for optimal parameters, called protected and greedy AFSA (PGAFSA), and a novel optimization target is also designed based on the aforementioned issues.

1) *Protected and Greedy Artificial Fish School Algorithm*: In general, X denotes the individual of artificial fish (AF), and the set $\{X_i\}$ represents the fish school. In this paper, $X = [k, R]$ represents the filtering parameters. The fitness function $Y = F(X_i)$ means the food concentration at the position of X_i .

Traditionally, the AFSA consists of three typical actions, including following, swarming, and preying, all of which are the limitation of fish's food-search behavior. Before taking action, the AF will evaluate and choose the best behavior. If it fails to find a suitable behavior, the AF will wander instead. Thus, there are two fatal problems in the classical method, i.e., a) the optimal solution is probably lost since a worse solution could be caused by the random prey action or the wandering behavior; and b) the evaluation stage costs time.

For higher efficiency, we provide strategies to solve the issues of optimum loss and time consumption.

- As for a common artificial fish (not the optimal individual), we build the greedy-following strategy, i.e., following a better one directly. If it fails, it will try to swarm. This strategy will make the search faster and reduce the time cost of behavior evaluation.
- For optimal artificial fish, the greedy-preying strategy is employed, i.e., the optimal individual obtains the found better solution directly in preying. As a result, the convergence speed will be enhanced and the optimum solution will not be lost during preying. Mathematically, the optimum is monotonically unabated.
- It is pronounced that wandering could possibly lead to optimum loss for the best individual. Therefore, the optimal fish is prohibited from wandering. Instead, we propose a staying behavior, i.e., holding its solution.

2) *Gradient-Based Histogram-Distribution Characteristics*: AFSA requires an appropriate fitness function as the food concentration. Thus, a comprehensive indicator ξ is proposed, namely Gradient-Based Histogram-Distribution Characteristics (GHC). According to the filtering-related attributes and the phenomenon described in Fig. 1, ξ is comprised of the haze indicator ψ , contrast indicator σ , and balance indicator μ , which can be formalized as follows:

$$\xi = \frac{\omega_\psi \psi \omega_\sigma \sigma}{1 + \omega_\mu \mu} \quad (11)$$

where $\omega_\mu, \omega_\psi, \omega_\sigma$ are corresponding weighted coefficients.

The haze indicator ψ is calculated with the average gradient in gray-scale map, and it describes the degree of haziness with gradient:

$$\psi = \overline{\text{Gradient}(p, t)^2} \quad (12)$$

where p is the pixel coordinate; The $\text{Gradient}(p, t)$ computes the gradient at a pixel p with $t \times 45^\circ$ as the direction. Obviously, ψ increases if the image becomes clear.

The balance indicator μ denotes the degree of color correction, and it equates the sum of the absolute difference of the average RGB-pixel values:

$$\mu = (|\mu_r - \mu_g| + |\mu_r - \mu_b| + |\mu_g - \mu_b|)/3 \quad (13)$$

where μ_λ denotes the average value, and μ decreases with the better color correction.

The contrast indicator σ is expressed by standard deviations of histogram distribution in RGB channels, which depicts the image contrast:

$$\sigma = \frac{1}{3} \sum_{\lambda} \text{Std}(hc_{\lambda}) \quad (14)$$

where hc_{λ} denotes the histogram distribution, and Std represents the standard deviation.

IV. FURTHER ADVANCEMENT AND GENERALIZATION WITH GANs

In this section, we first introduce the architecture of the proposed GAN-RS for underwater image restoration. Then, we explain in detail how to construct the objective.

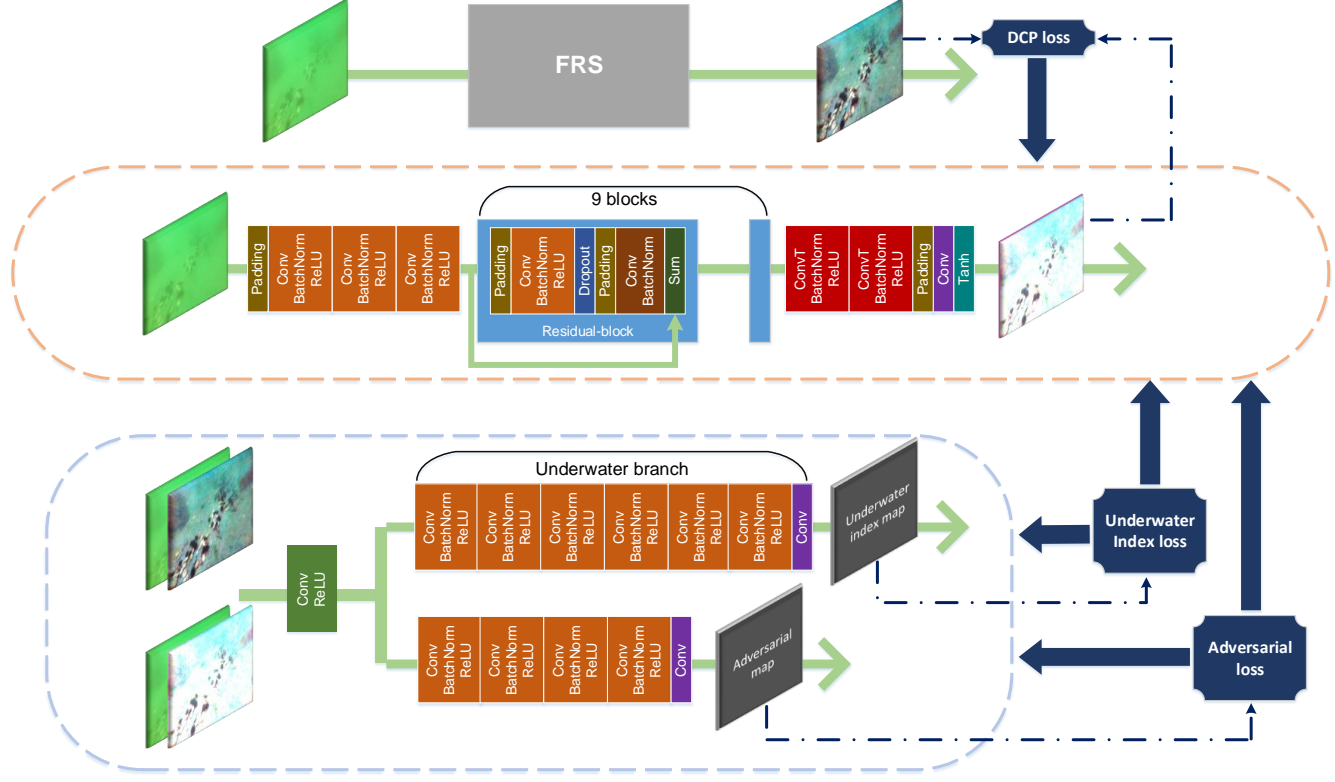


Fig. 2. Architecture of GANs developed in this paper. From top to bottom: the FRS, the generator, and the discriminative model.

A. Architecture

As illustrated in Fig. 2, the proposed architecture includes the generative and discriminative models, and the discriminator contains the adversarial branch and the underwater branch.

The architecture of generator in this paper follows [24], which is composed of residual blocks [32]. By means of the 9-residual-block stack, the downsample-upsample model learns the essence of the input scene, and then, the clear version will emerge in the original resolution after deconvolution operations.

We design the discriminator with a multi-branch framework, and the original real-or-fake discrimination is realized by the adversarial branch. For underwater application, the underwater branch is carefully designed to learn underwater attributes. That is, in addition to performing traditional discrimination, D also predicts the underwater probability. More specifically, designed with a stack of Conv-BatchNorm-ReLU (CBR) unit [25], the underwater branch discern whether an image belongs to underwater scene. Inspired by the PatchGANs [25], we design all the discriminator in the idea of ‘‘Patch’’. Since the discrimination of underwater attributes requires more contextual information, more CBR units are employed in underwater branch for larger receptive field. Equipped with 6 CBR units, the size of underwater index map is 6×6 and the size of receptive field is 286×286 . Correspondingly, the adversarial branch is constructed with 2 less CBR units, so the sizes change to 30×30 and 70×70 , respectively.

B. Objective and Training Strategy

The operation of the adversarial and underwater branches in the discriminator are denoted by D_a and D_u , respectively.

1) *Adversarial Loss*: As the input condition, the original underwater image fed to G is denoted as x , and G generates y with a noise z , i.e., $G(x, z) \rightarrow y$. Original conditional adversarial loss is a sigmoid cross entropy:

$$\begin{aligned} \mathcal{L}_{cGAN} = & \mathbb{E}_{x, y \sim p_{data}(x, y)} [\log D_a(x, y)] \\ & + \mathbb{E}_{x \sim p_{data}(x), z \sim p_z(z)} [\log(1 - D_a(x, G(x, z)))] \end{aligned} \quad (15)$$

The generator G tries to minimize the objective while D attempts to maximize it. Hence, we have $G^* = \arg \min_G \max_D \mathcal{L}_{cGAN}(G, D)$. However, Mao *et al.* stated that (15) may lead to the vanishing gradients problem during the training process, and they advocated the Least Squares Generative Adversarial Networks (LSGANs) [39], whose loss function is the least squares form:

$$\begin{cases} \mathcal{L}_{lscGAN_D} = \mathbb{E}_{x, y \sim p_{data}(x, y)} [(D_a(x, y) - a)^2] \\ + \mathbb{E}_{x \sim p_{data}(x), z \sim p_z(z)} [(D_a(x, G(x, z)) - b)^2] \\ \mathcal{L}_{lscGAN_G} = \mathbb{E}_{x \sim p_{data}(x), z \sim p_z(z)} [(D_a(x, G(x, z)) - a)^2] \end{cases} \quad (16)$$

In this paper, LSGANs is employed for high training efficiency, and $a = 1, b = 0$ are the labels of the real or synthesized data, respectively.

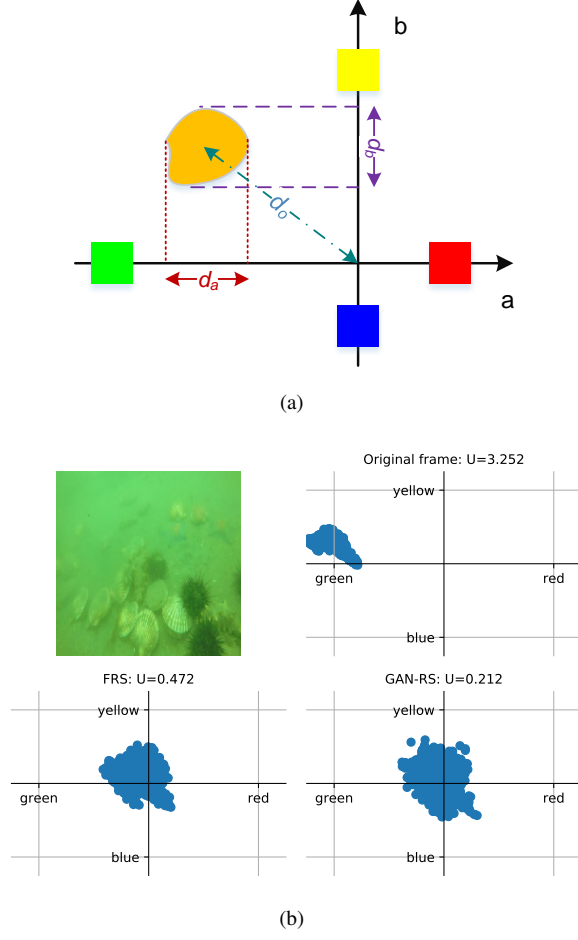


Fig. 3. Illustration of the underwater index. (a) The diagram of the underwater index; (b) The experiment results.

2) *DCP Loss*: To promote the generator not only fool the discriminator but also encourage the output to close to the ground truth at the pixel level, a *L1* loss between y and $G(x, z)$ is employed in pix2pix [25]. Since our task is not a traditional image-to-image translation, we design a DCP loss for the same purpose based on the knowledge that there is a distinctively distinguishable appearance among hazy or clear images in the dark channel [9]. In particular, we simplify the patch Ω as a pixel p :

$$\begin{cases} y_{dark}^{rgb}(p) = \min_{\lambda \in \{r, g, b\}} y_{\lambda}(p) \\ G(x, z)_{dark}^{rgb}(p) = \min_{\lambda \in \{r, g, b\}} G(x, z)_{\lambda}(p) \\ \mathcal{L}_{DCP} = \mathbb{E}_{x, y \sim p_{data}(x, y), z \sim p_z(z)} \|y_{dark}^{rgb} - G(x, z)_{dark}^{rgb}\| \end{cases} \quad (17)$$

3) *Underwater Index Loss*: In order to improve the visual quality further on the basis of the ground truth produced by the FRS, a novel loss function is proposed to train underwater branch, namely underwater index loss. According to the massive-data observation, we deem that there is a distinctive characteristic of underwater image in Lab color space. As shown in Fig. 3(a), the Lab color space has strong capability of indicating color distribution, i.e., the red and green can be clearly differentiated on a -axis while blue and yellow versa.

Moreover, as shown by the orange patch in Fig. 3(a), the $a - b$ scatters of underwater scene always gather far away from the origin while that of an in-air image usually distribute sparsely centered by the origin. Thus, three distances, i.e., d_a , d_b , and d_o in Fig. 3(a), can be used to formulate the underwater possibility of an image. Accordingly, the underwater index is defined as:

$$U = \frac{\sqrt{d_o}}{10a_l d_a d_b} \quad (18)$$

where a_l denotes the average value of L-channel, and the square root for d_o is employed for the purpose of amplifying the small distance.

Next, the underwater index loss is designed, which will be learned with *L2* sense by the underwater branch:

$$\begin{cases} \mathcal{L}_{UD} = \mathbb{E}_{y \sim p_{data}(y)} [(D_u(y) - U(y))^2] \\ + \mathbb{E}_{x \sim p_{data}(x), z \sim p_z(z)} [(D_u(G(x, z)) - U(G(x, z)))^2] \\ \mathcal{L}_{UG} = \mathbb{E}_{z \sim p_z(z)} [(D_u(G(x, z)))^2] \end{cases} \quad (19)$$

For the idea of ‘‘Patch’’, we develop the patch underwater index loss regarding receptive field. The size and bounding box position of RF are calculated following [40].

4) *Full Objective*: The full objective is

$$\begin{cases} \mathcal{L}_D = \omega_{GAN} \mathcal{L}_{lscGAN_D} + \omega_U \mathcal{L}_{UD} \\ \mathcal{L}_G = \omega_{GAN} \mathcal{L}_{lscGAN_G} + \omega_U \mathcal{L}_{UG} + \omega_{DCP} \mathcal{L}_{DCP} \end{cases} \quad (20)$$

where $\omega_{GAN}, \omega_U, \omega_{DCP}$ are the weighted coefficients, and the optimal models are formulated as $D^* = \arg_D \min \mathcal{L}_D, G^* = \arg_G \min \mathcal{L}_G$.

5) *Multi-Stage Loss Strategy*: The initial underwater branch is not able to discern anything. Thus, we let $\mathcal{L}_G = \omega_{GAN} \mathcal{L}_{lscGAN_G} + \omega_{DCP} \mathcal{L}_{DCP}$ at the beginning of training. Then, $\omega_U \mathcal{L}_{UG}$ will be allied to \mathcal{L}_G after 30 epoches, when the underwater branch has been well trained.

Fig. 4(a) illustrates the training process after \mathcal{L}_{UG} is allied to \mathcal{L}_G , in which the 30-epoch result is quite similar to the output of FRS while the underwater index has not been controlled effectively. In the next step, underwater branch begins to guide the generator, so U decreases quickly in 35 epoch. The adversarial loss, on the contrary, increases to some extent. Both of the loss functions will contribute to the generated data. That is, dominating the training of G , the adversarial branch and underwater branch alternately work as the leader, and they will reach balance when G finds a compromise.

V. EXPERIMENTS AND ANALYSES

We at first unveil the implementation of the GAN-RS and the training process. Then, the time efficiency is tested. For comprehensive performance comparison, the FRS and the GAN-RS is compared with existing methods on restoration quality and applications. Finally, we also discuss the proposed algorithms.

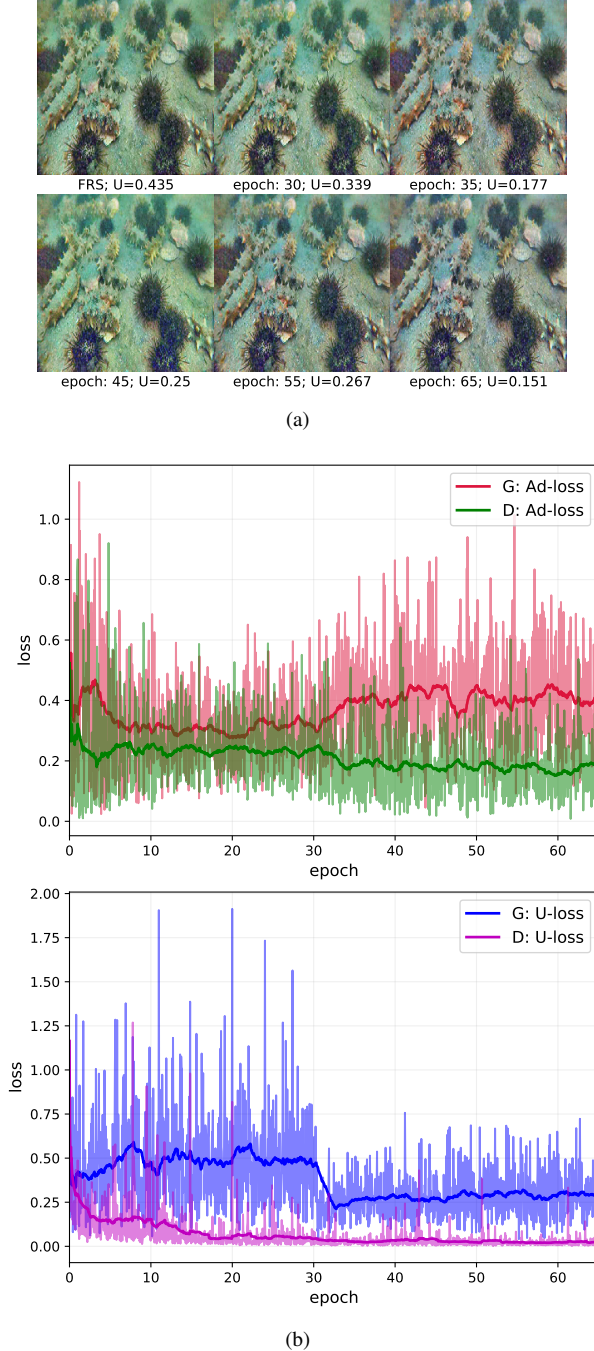


Fig. 4. Illustration of the training process. (a) The training process after \mathcal{L}_{U_G} works; (b) The loss curves. Ad-loss denotes the \mathcal{L}_{lscGAN} while U-loss represents the \mathcal{L}_U .

A. Implementation and Training Details

1) *Basic Setting*: By collecting practical underwater images in seafood breeding base in Zhangzidao and Qingdao, China, the dataset is established with 2201 frames as the training set while the test set combines our data with public underwater images. Our training setting follows what provided by DCGAN [20]. The leaning rate is stared with 0.0002, and a linear decay is employed after 50 epoches. The Adam solver with the parameters of $\beta = [0.50, 0.99]$, $\epsilon = 10^{-8}$ is employed as the optimizer [41]. In particular, both the input

and output resolution is 512×512 ; batch size is fixed to 2, and $\omega_{GAN} = 1$, $\omega_U = 10$, $\omega_{DCP} = 30$ in this paper. More specifically, the discriminator is trained one step with the synthesized data or the real data randomly, rather than their combination.

2) *Running Environment*: Our method is implemented under the PyTorch framework. On the other hand, our training as well as experiments are carried out on a workstation with one Intel Xeon(R) E5-2630 2.20 GHz CPU, two NVIDIA TITAN-Xp GPUs, and 64 G RAM.

3) *Multi-Stage Training Process*: The loss curves are illustrated in Fig. 4(b). the stair in \mathcal{L}_{U_G} is evident, i.e., the underwater branch goes into effect after 30 epoches. Moreover, in terms of adversarial loss, it can be seen that G, D have achieved dynamic equilibrium in the early training, but \mathcal{L}_{GAN} deviates from the balance point when \mathcal{L}_{U_G} works. That is, the generated image is deemed that it has higher probability to be synthesized by D while D is more confident about its discrimination. Gradually, a new dynamic equilibrium will be obtained at another pair of balance point, e.g., \mathcal{L}_{GAN_D} is stable at > 0.2 while < 0.2 during the early and final training, respectively. Note that the dynamic equilibrium may be broken, if ω_U or ω_{GAN} is out of tune.

B. Under-Sea Maneuver and Time Efficiency Test

Based on a platform of remotely operated vehicle (ROV), we conduct the practical experiments on the seabed. Equipped with a camera as the visual guidance, the ROV is 0.68 m in length, 0.57 m in width, 0.39 m in height, and 50 kg in weight. The test venue is located at Zhangzidao, Dalian, China, where the water depth is approximately 10 m. Due to space limitation, the interested readers may refer to the attached experimental video (also available at <https://www.youtube.com/watch?v=JKCedUhAM6M>). It should be noted that all video data comes from the first Underwater Robot Picking Contest (Dalian, China, Sep. 19–23, 2017, available at <http://www.cnurpc.org>).

The time efficiency and optimal-parameter analysis in the phase of the FRS pre-search are detailed in [36]. In this paper, the time-related data are obtained with a 512×512 -pixel-size and 1699-frame video. The average processing speed for the FRS is 118.56 fps after pre-search while the GAN-RS achieves 133.77 fps, both of which is far more superior to existing restoration methods. Thus, when employed in some comprehensive application tasks, e.g., underwater object detection, the FRS and the GAN-RS have a neglectable effective on realtimeness.

C. Quantitative Comparison

1) *Underwater Index Test*: As illustrated in Fig. 3(b), underwater index is presented graphically. The image illustrates a typical underwater scene, which is so hazy and color-distorted that objects are hard to emerge. The upper right corner shows the color distribution in $a - b$ plane. As can be seen, the color distortion is reflected in the distance between distribution center and the origin, i.e., d_o is large for terrible color distortion. On the other hand, the haziness is related

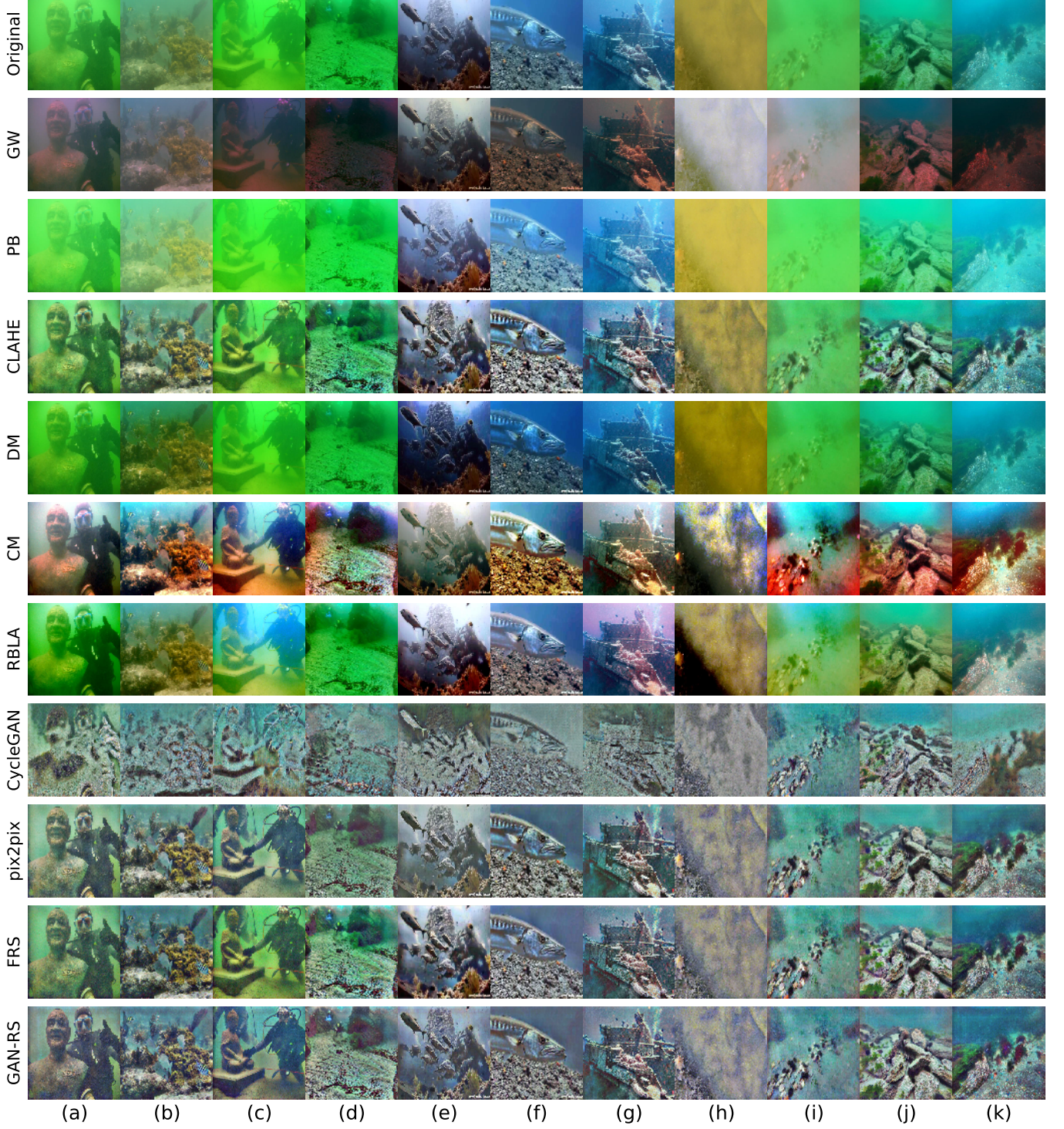


Fig. 5. Comparison between our methods with others. (a)–(c) are from [8]; (d) is from [49]; (e)–(f) are from [6]; (g) is from [13]; and the other are ours.

to the concentration degree of the distribution. For brevity, $d_a d_b$ approach to 0 owing to haziness or lower contrast. Thus, $U \rightarrow 0$ is the ideal condition. Though it is not involved in the optimization, the FRS performs well to enhance the underwater index. As shown in the lower left corner of Fig. 3(b), the distribution in $a - b$ plane is improved to a large extent. Further, the GAN-RS uses underwater branch to decrease the underwater index loss. As illustrated in the

lower right corner of Fig. 3(b), a more considerable U can be achieved with the less bias and greater dispersibility in the $a - b$ plane. Therefore, the proposed underwater index has the capability of describing the probability whether an image is aquatic, and it is effective when employed as an evaluator for underwater vision restoration.

2) *Quality Comparison*: In this section, the proposed methods are compared with the GW [5], CLAHE [7], Probability-

TABLE I
QUANTITATIVE COMPARISON USING NO-REFERENCE QUALITY ASSESSMENT

Label	Figure	d_o	$d_a d_b$	U	Laplace	Entropy	UCIQE	UICM	UISM	UIConM	UIQM
(a)	Original	0.79	0.04	3.60	3.11	6.93	0.42	-0.63	3.19	0.15	1.45
	GW	0.51	0.25	0.53	2.03	6.54	0.45	2.83	1.75	0.12	1.02
	PB	0.84	0.03	3.76	2.12	6.47	0.36	-2.01	1.83	0.10	0.85
	CLAHE	0.58	0.11	0.97	8.21	7.22	0.49	1.11	11.83	0.17	4.13
	DM	0.79	0.04	3.95	2.72	6.91	0.45	0.06	3.26	0.13	1.43
	RBLA	0.63	0.13	1.02	3.93	7.51	0.57	2.21	5.75	0.15	2.30
	pix2pix	0.35	0.15	0.47	16.50	7.23	0.49	2.20	13.87	0.21	4.90
	FRS	0.36	0.14	0.51	23.10	7.24	0.51	2.51	14.42	0.21	5.07
	GAN-RS	0.22	0.2	0.25	17.96	7.15	0.50	2.63	14.20	0.21	5.01
(i)	Original	0.85	0.02	5.56	1.16	4.83	0.29	-1.73	0.66	0.08	0.45
	GW	0.75	0.24	0.56	1.48	4.59	0.36	2.60	0.82	0.07	0.57
	PB	0.86	0.01	9.8	0.99	4.17	0.27	-2.27	0.28	0.05	0.20
	CLAHE	0.77	0.13	0.94	3.14	5.95	0.38	-0.35	4.17	0.13	1.67
	DM	0.85	0.04	3.09	1.60	5.30	0.34	-0.79	0.97	0.09	0.58
	RBLA	0.71	0.21	0.54	3.01	6.13	0.46	4.13	3.90	0.12	1.69
	pix2pix	0.33	0.25	0.24	14.04	6.87	0.52	2.71	14.18	0.20	5.00
	FRS	0.28	0.26	0.2	15.42	6.99	0.54	3.11	14.25	0.20	5.02
	GAN-RS	0.27	0.27	0.19	15.72	6.94	0.53	2.30	14.34	0.20	5.03
(k)	Original	0.74	0.04	4.28	6.22	6.49	0.42	0.14	6.47	0.17	2.51
	GW	0.53	0.13	2.65	3.26	5.28	0.49	4.43	3.55	0.14	1.68
	PB	0.83	0.05	2.64	4.28	6.13	0.36	-0.52	5.92	0.12	2.17
	CLAHE	0.49	0.17	0.59	19.70	7.01	0.53	3.83	11.63	0.17	4.15
	DM	0.72	0.05	3.45	6.27	6.43	0.42	0.06	6.03	0.14	2.27
	RBLA	0.53	0.12	0.92	10.65	7.03	0.55	7.03	8.86	0.16	3.38
	pix2pix	0.35	0.23	0.36	24.76	7.09	0.56	4.08	12.76	0.20	4.60
	FRS	0.28	0.19	0.34	25.12	7.13	0.57	4.02	13.42	0.20	4.79
	GAN-RS	0.3	0.27	0.25	28.80	7.06	0.57	4.19	13.57	0.21	4.86
Average	Original	0.66	0.05	2.81	4.77	6.46	0.44	0.26	5.56	0.15	2.20
	GW [5]	0.51	0.16	1.28	3.52	6.03	0.46	3.03	4.24	0.13	1.80
	PB [44]	0.73	0.06	2.51	3.67	6.11	0.40	-0.46	5.02	0.11	1.87
	CLAHE [7]	0.48	0.14	0.69	12.28	7.11	0.52	2.35	11.33	0.16	3.98
	DM [10]	0.64	0.07	2.32	4.69	6.44	0.46	0.99	5.52	0.14	2.14
	RBLA [14]	0.51	0.12	0.93	7.10	7.11	0.56	3.93	8.30	0.15	3.09
	pix2pix [25]	0.25	0.18	0.32	20.51	7.18	0.53	2.74	13.58	0.20	4.79
	FRS	0.26	0.19	0.30	23.85	7.26	0.55	3.14	13.75	0.20	4.85
	GAN-RS	0.19	0.21	0.20	22.95	7.19	0.54	2.83	13.87	0.20	4.88

based method (PB) [44], CycleGAN [28], pix2pix [25], RBLA [14], and the dehazing (DM) or contrast enhancement method (CM) in [10]. The comparison is demonstrated in Fig. 5, verifying the qualitative superiority of the proposed FRS and GAN-RS. Compared against several prior and contemporary methods, our approaches achieve the clear vision, balanced color, stretched contrast, and more details. Some approaches restore underwater environment on one hand, e.g., the GW only achieves white balance; the CLAHE has ignorable effect on color correction; and the brightness advancement introduced by the PB comes with the aggravation of the color distortion. Meanwhile, our methods hardly destroy the original information of an image. On the contrary, the CycleGAN cannot maintain the semantic content for lack of supervision while the CM could not preserve the objective color for an image in some cases. For example, some CM processed images look excessively reddish, see (i)–(k). The RBLA performs well, but there is a drawback that the parameter adjustment is complex and empirical. For instance, the RBLA restores underwater image with 404×303 as the resolution in the original paper [14]. In this paper, 512×512 images, instead, are fed to it. As a result, its performance is restricted when the original parameters are maintained. The numerical comparison is shown in Table I. There is no in-air ground truth for comparison, so some no-reference quality assess-

ment tools are employed, including the underwater index, the Laplace gradient, the entropy, Underwater Color Image Quality Evaluation Metric (UCIQE) [47], and Underwater Image Quality Measure (UICM, UISM, UIConM, UIQM) [48]. The underwater index proposed in this paper can be treated as the probability whether a scene belongs to underwater location or not. The Laplace gradient reflects the haze degree of an image while the entropy denotes the richness of image information. The UIQM, composed of UICM, UISM, UIConM, represents the comprehensive quality of a restored underwater image, and its sub-indexes are the pros-and-cons quantization of color, sharpness, and contrast, respectively. Similarly, UCIQE quantifies image quality via chrominance, average saturation, and luminance contrast. Note that the CycleGAN and CM are not involved in Table I owing to the aforementioned drawback.

As shown in Table I, the data include three typical underwater environments and the average among the test set. Some methods work well on a particular perspective, e.g., the GW is effective against color distortion. On the other hand, the production of the RBLA is the best for the UCIQE followed by the FRS and the GAN-RS with a small gap of 0.01. In terms of underwater index, it is interesting that the pix2pix can hardly perform better than its ground truth (FRS), but the GAN-RS achieve a great improvement on d_o , $d_a d_b$, and U thanks to the underwater branch. As for the UIQM, the

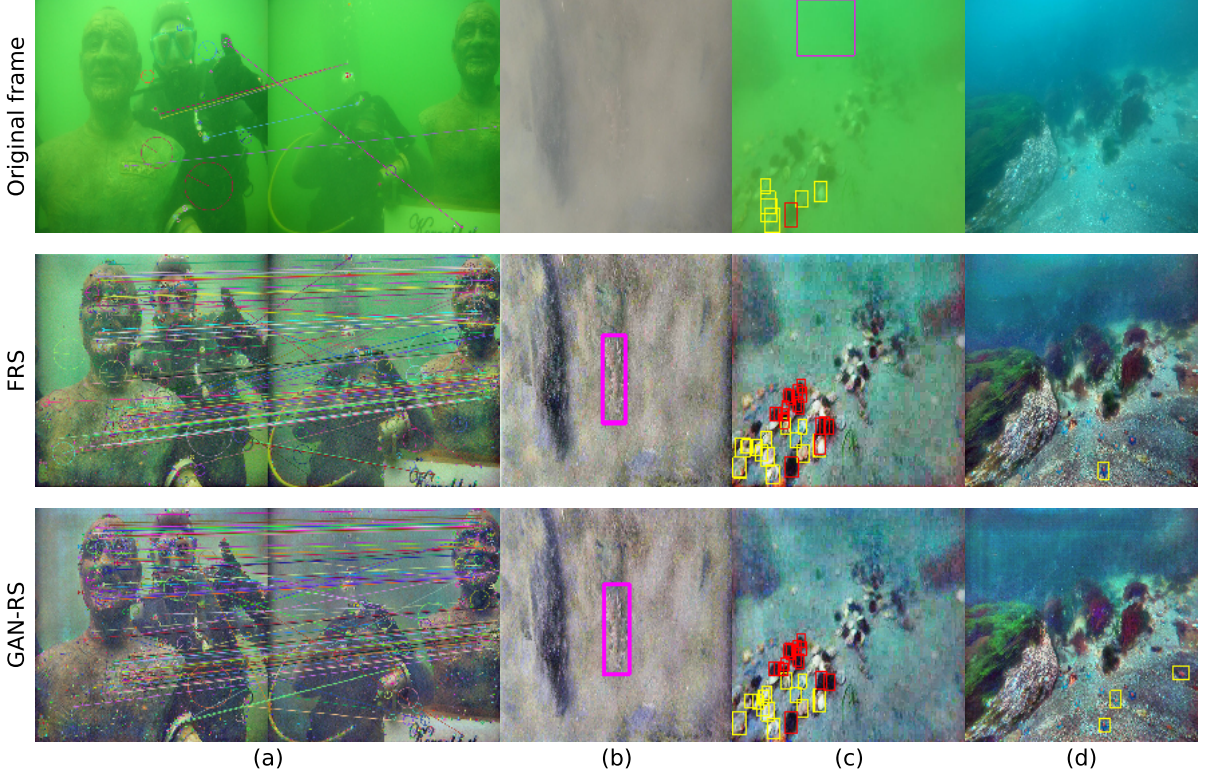


Fig. 6. Application test with the SIFT and the SSD.

FRS generates the UICM-optimal outputs, and the GAN-RS is better on UISM, UIConM, and UIQM.

Therefore, the conclusion can be drawn based on the comparison that the comprehensive performance of the proposed GAN-RS is better in terms of the restoration quality. Namely, it is capable of not only color correction, but also contrast stretch. In the meantime, the sharpness of underwater images can benefit from the GAN-RS.

D. Application Tests

In this section, some feature-related algorithms including SIFT [42], Harris [46], Canny [45], and SSD [43] are employed to test the application of the FRS and the GAN-RS from the perspectives of the fundamental features and object detection. Consistent with the previous comparison, the test set contains the public data, the terribly hazy environments, and the greenish or bluish scenes, whose samples are shown in Fig. 6(a)–(d), respectively. The SIFT match, at first, is utilized to test the proposed methods. As shown in Fig. 6(a), few key points can be obtained by the SIFT in the original frame, and there is seldom a match. On the contrary, assisted by the proposed algorithms, salient features are extracted, and a multitude of matches appear. Note that the SIFT draws more key points with the GAN-RS than that with the FRS, revealing that the GAN-RS is more efficient.

For object detection, the SSD is employed to locate targets in a frame. Our SSD model is trained by the aforementioned datasets, and the training data contains the original frames and the various-parameter-FRS processed version. As shown

in Fig. 6(b)–(d), the SSD is leveraged for the targets of trepang, shell, urchin, and starfish. However, if it works on the original scene, the SSD struggles with recall rate and precision. By contrast, the performance of SSD dramatically improves, if facilitated by the FRS or the GAN-RS.

The numerical comparison is shown in Table II, by which the scene-irrelevant superiority of the FRS and the GAN-RS are revealed. By comparison, the SIFT and the Harris perform better combining with the GAN-RS while the output of the FRS covers more edges. Moreover, the recall rate and precision of SSD are promoted more rapidly with the assistance of the proposed approaches. Therefore, it is verified that the proposed FRS and GAN-RS contribute to the extraction of fundamental and high-level features of underwater images.

E. Discussion

The CNNs architecture is able to learn from big data, mapping a sample to the target. In general, the CNNs can hardly be more superior to its supervisor. We develop the GAN-RS in this paper for the purpose of quality advancement of underwater machine vision, and the FRS is employed as the supervisor. For the specific task, the underwater index loss and underwater branch are designed to ensure that the GAN-RS can perform better. However, the FRS is not irreplaceable since there are many other restoration algorithms for underwater vision. That is, the GAN-RS can learn from any methods, and even multiple algorithms. Further, the GAN-RS can generalize and accelerate what it learns. Thus, if the training data is extensive enough, any underwater environment could be dealt

TABLE II
RESULTS OF APPLICATION TESTS

Label	Figure	Recall	Precision	SIFT	Harris	Canny
(a)	Original	-	-	61	0	0.00
	GW	-	-	20	0	0.00
	PB	-	-	20	0	0.00
	CLAHE	-	-	628	278	0.04
	DM	-	-	94	12	0.00
	CM	-	-	373	227	0.03
	RBLA	-	-	256	121	0.20
	pix2pix	-	-	1732	1522	0.11
	FRS	-	-	1154	1652	0.18
(b)	GAN-RS	-	-	1804	1633	0.14
	Original	0	0	1	0	0.00
	GW	0	0	6	0	0.00
	PB	0	0	0	0	0.00
	CLAHE	0	0	82	49	0.00
	DM	0	0	144	109	0.01
	CM	1	0.67	719	589	0.06
	RBLA	0	0	169	206	0.01
	pix2pix	1	1	1201	1700	0.09
(c)	FRS	1	1	1286	1994	0.21
	GAN-RS	1	1	1377	1673	0.18
	Original	0.16	0.86	8	0	0.00
	GW	0.04	0.50	17	14	0.00
	PB	0.12	0.83	1	0	0.00
	CLAHE	0.53	0.89	168	172	0.01
	DM	0.20	0.91	26	10	0.00
	CM	0.02	0.67	755	895	0.06
	RBLA	0.14	0.86	90	150	0.01
(d)	pix2pix	0.55	0.90	1201	1700	0.09
	FRS	0.59	1	1562	2138	0.16
	GAN-RS	0.53	1	1708	1941	0.12
	Original	0	0	241	339	0.02
	GW	0	0	129	371	0.02
	PB	0	0	243	325	0.01
	CLAHE	0.15	1	2010	2251	0.16
	DM	0	0	488	543	0.03
	CM	0.08	0.5	1497	1341	0.15
ave	RBLA	0.15	1	938	1056	0.09
	pix2pix	0.08	1	1840	2077	0.15
	FRS	0.08	1	1789	1886	0.15
	GAN-RS	0.23	1	2005	2494	0.17

Recall, Precision: the recall rate and precision for SSD detection with 0.2 as the confidence threshold

SIFT: the number of SIFT key points;

Harris: the number of Harris corners;

Canny: the pixel-level edge ratio in an image;

ave: the average value.

with at a high frame rate without any empirical parameter adjustment.

The limitations of GAN-RS are twofold. On the one hand, the training data is demanded for a variety of underwater environments. The GAN-RS can hardly work well on some samples, whose data distribution is far away from the training set, and there is no chance to make up by parameter adjustment. For example, it is impossible to obtain a clear version, if a reddish underwater image is fed to the GAN-RS, because the collected training set does not cover some analogical

environments. On the other hand, the training parameters need to be carefully set or adjusted. The generative model will bring extra periodic noise or bad blocks in output images, if trained with an improper setting.

VI. CONCLUSION AND FUTURE WORK

This paper has taken aim to adaptively restore underwater image in real time, and the FRS and the GAN-RS are creatively proposed. Different from the IFM-based methods, the FRS restores underwater images in frequency domain, and the dehazing and color correction are based on filtering. In order to seek optimal parameters, PGAFSA is developed with GHC as its target. By means of neural networks, the GANs is leveraged to make more progress in this paper. For further advancement, the discriminator is equipped with a crafted underwater branch, and the underwater index is designed according to the underwater attributes. Combining with the adversarial loss, DCP loss, and underwater index loss, the generative model obtains a correct guidance to produce a clear image. Moreover, the multi-stage loss strategy is employed to harness the training process. As a breakthrough, the proposed GAN-RS restores underwater scenes at a high frame rate without any requirement of information estimation or parameter search. In addition, both qualitative and quantitative comparisons on image quality and applications are conducted. Finally, the GAN-RS achieves superior comprehensive performance on the color correction, contrast stretch, dehazing, and detail or feature restoration compared with traditional methods.

In the future, we plan to investigate the underwater object detection and motion estimation based on the proposed GAN-RS. Of course, more practical experiments will be carried out for real-world underwater applications.

ACKNOWLEDGMENT

The authors would like to thank Chong-Yi Li and Yan-Tsung Peng for providing the source codes of the DM, CM, and RBLA.

REFERENCES

- [1] D. Chen, X. Chu, F. Ma, and X. Teng, "A variational approach for adaptive underwater sonar image denoising," in *Proc. Int. Conf. Transport. Inform. Safety*, Banff, Canada, Aug. 2017, pp. 1177–1181.
- [2] Y. Zhang, Y. G. H. Wei, L. Lou, H. Song, P. Yang, and C. Liu, "Influence of water on underwater distance measurement by a laser range finder," in *Proc. IEEE/MTS Ocean.*, Aberdeen, Scotland, Jun. 2017, pp. 1–5.
- [3] M.-C. Chuang, J.-N. Hwang, K. Williams, and R. Towler, "Tracking live fish from low-contrast and low-frame-rate stereo videos," *IEEE Trans. Circuits Syst. Video Technol.*, vol. 25, no. 1, pp. 167–179, 2015.
- [4] D. Lee, G. Kim, D. Kim, H. Myung, and H.-T. Choi, "Vision-based object detection and tracking for autonomous navigation of underwater robots" *Ocean Eng.*, vol. 48, pp. 59–68, 2012.
- [5] E. Provenzi, C. Gatta, M. Fierro, and A. Rizzi, "A spatially variant white-patch and gray-world method for color image enhancement driven by local contrast," *IEEE Trans. Pattern Anal. Mach. Intell.*, vol. 30, no. 10, pp. 1757–1770, 2008.
- [6] J.-Y. Chiang and Y. Chen, "Underwater image enhancement by wavelength compensation and dehazing," *IEEE Trans. Image Process.*, vol. 21, no. 4, pp. 1756–1769, 2012.
- [7] K. Zuiderveld, "Contrast limited adaptive histogram equalization," in *Graphics gems IV*, pp. 474–485, 1994.
- [8] C. Ancuti, C. O. Ancuti, T. Haber, and P. Bekaert, "Enhancing underwater images and videos by fusion," in *Proc. IEEE Conf. Comput. Vis. Pattern Recognition*, Providence, Rhode Island, Jun. 2012, pp. 81–88.

[9] K. He, J. Sun, and X. Tang, "Single image haze removal using dark channel prior," *IEEE Trans. Pattern Anal. Mach. Intell.*, vol. 33, no. 12, pp. 2341–2353, 2011.

[10] C. Li, J. Guo, R. Cong, Y. Pang, and B. Wang, "Underwater image enhancement by dehazing with minimum information loss and histogram distribution prior," *IEEE Trans. Image Process.*, vol. 25, no. 12, pp. 5664–5677, 2016.

[11] Y.-Y. Schechner and N. Karpel, "Clear underwater vision," in *Proc. IEEE Conf. Comput. Vis. Pattern Recognition*, Washington, USA, Jun. 2004, pages I-536–I-543.

[12] B.-L. McGlamery, "A computer model for underwater camera systems," *Ocean Optics VI*, vol. 208, pp. 221–232, 1980.

[13] S. Emberton, L. Chittka, and A. Cavallaro, "Hierarchical rank-based veiling light estimation for underwater dehazing," in *Proc. Brit. Mach. Vis. Conf.*, Swansea, the UK, Sep. 2015, pp. 125.1–125.12.

[14] Y.-T. Peng and P. C. Cosman, "Underwater image restoration based on image blurriness and light absorption," *IEEE Trans. Image Process.*, vol. 26, no. 4, pp. 1579–1594, 2017.

[15] E.-P. Bennett, J.-L. Mason, and L. McMillan, "Multispectral bilateral video fusion," *IEEE Trans. Image Process.*, vol. 16, no. 5, pp. 1185–1194, 2007.

[16] L. Xu, Q. Yan, Y. Xia, and J. Jia, "Structure extraction from texture via relative total variation," *ACM Trans. Graph. SIGGRAPH Asia*, vol. 31, no. 6, pp. 1–139, 2012.

[17] Y.-S. Shin, Y. Cho, G. Pandey, and A. Kim, "Estimation of ambient light and transmission map with common convolutional architecture," in *Proc. IEEE/MTS Ocean*, Monterey, USA, Sep. 2016, pp. 1–7.

[18] I. Goodfellow, J. Pouget-Abadie, M. Mirza, B. Xu, D. Warde-Farley, S. Ozair, and Y. Bengio, "Generative adversarial nets," in *Proc. Adv. in Neural Info. Proc. Syst.*, Montreal, Canada, Dec. 2014, pp. 2672–2680.

[19] M. Mirza and S. Osindero, "Conditional generative adversarial nets," *arXiv:1411.1784*, 2014.

[20] A. Radford, L. Metz, and S. Chintala, "Unsupervised representation learning with deep convolutional Generative Adversarial Networks," *arXiv:1511.06434*, 2015.

[21] C. Li and M. Wand, "Precomputed real-time texture synthesis with markovian generative adversarial networks," in *Proc. Eur. Conf. Comput. Vis.*, Amsterdam, Netherlands, Oct. 2016, pp. 702–716.

[22] J.-Y. Zhu, P. Krakenbuhl, E. Shechtman, and A.-A. Efros, "Generative visual manipulation on the natural image manifold," in *Proc. Eur. Conf. Comput. Vis.*, Amsterdam, Netherlands, Oct. 2016, pp. 597–613.

[23] J. Johnson, A. Alahi, and L. Fei-Fei, "Perceptual losses for real-time style transfer and super-resolution," in *Proc. Eur. Conf. Comput. Vis.*, Amsterdam, Netherlands, Oct. 2016, pp. 694–711.

[24] C. Ledig, L. Theis, F. Huszár, J. Caballero, A. Cunningham, A. Acosta, and W. Shi, "Photo-realistic single image super-resolution using a generative adversarial network," *arXiv:1609.04802*, 2016.

[25] P. Isola, J.-Y. Zhu, T. Zhou, and A.-A. Efros, "Image-to-image translation with conditional adversarial networks," *arXiv:1611.07004*, 2016.

[26] C. Wang, C. Xu, C. Wang, and D. Tao, "Perceptual adversarial networks for image-to-image transformation," *arXiv:1706.09138*, 2017.

[27] H. Dong, P. Neekhara, C. Wu, and Y. Guo, "Unsupervised image-to-image translation with generative adversarial networks," *arXiv:1701.02676*, 2017.

[28] J.-Y. Zhu, T. Park, P. Isola, and A.-A. Efros, "Unpaired image-to-image translation using cycle-consistent adversarial networks," *arXiv:1703.10593*, 2017.

[29] Z. Yi, H. Zhang, and P.-T. Gong, "DualGAN: Unsupervised dual learning for image-to-image translation," *arXiv:1704.02510*, 2017.

[30] O. Ronneberger, P. Fischer, and T. Brox, "U-net: Convolutional networks for biomedical image segmentation," in *Proc. Int. Conf. Medical Image Computing Computer-Assisted Intervention*, Munich, Germany, Oct. 2015, pp. 234–241.

[31] K. Simonyan and A. Zisserman, "Very deep convolutional networks for large-scale image recognition," *arXiv:1409.1556*, 2014.

[32] S. Gross and M. Wilber, "Training and investigating residual nets," Feb. 2016. [Online]. Available: <http://torch.ch/blog/2016/02/04/resnets.html>.

[33] W. Lai, J. Huang, and M. Yang, "Semi-supervised learning for optical flow with generative adversarial networks" in *Proc. Adv. in Neural Info. Proc. Syst.*, Long Beach, USA, Dec. 2017, pp. 353–363.

[34] J. Li, K.-A. Skinner, R.-M. Eustice, and M. Johnson-Roberson, "WaterGAN: Unsupervised generative network to enable real-time color correction of monocular underwater images," *IEEE Robot. Autom. Lett.*, vol. 3, no. 1, pp. 387–394, 2018.

[35] C. Li, J. Guo, and C. Guo, "Emerging from water: Underwater image color correction based on weakly supervised color transfer," *arXiv:1710.07084*, 2017.

[36] X. Chen, Z. Wu, J. Yu, and L. Wen, "A real-time and unsupervised advancement scheme for underwater machine vision," in *Proc. IEEE Int. Conf. Cyber Technol. Autom., Control, Intell. Syst.*, Hawaii, USA, Aug. 2017, pp. 271–276.

[37] R. Hufnagel and N. Stanley, "Modulation transfer function associated with image transmission through turbulent media," *J. Opt. Soc. Am.*, vol. 54, no. 1, pp. 52–60, 1964.

[38] Y. Zhou and H. Huang, "Hybrid artificial fish school algorithm based on mutation operator for solving nonlinear equations," in *Proc. Int. Workshop Intell. Syst. Appl.*, Wuhan, China, May, 2009, pp. 1–5.

[39] X. Mao, Q. Li, H. Xie, R.-Y. Lau, Z. Wang, and S.-P. Smolley, "Least squares generative adversarial networks," *arXiv:1611.04076*, 2016.

[40] Z. Cheng, F. Bai, Y. Xu, G. Zheng, S. Pu, and S. Zhou, "Focusing attention: Towards accurate text recognition in natural images," *arXiv:1709.02054*, 2017.

[41] D. Kingma and J. Ba, "Adam: A method for stochastic optimization," *arXiv:1412.6980*, 2014.

[42] D.-G. Lowe, "Distinctive image features from scale-invariant keypoints," *Int. J. Comput. Vis.*, vol. 60, no. 2, pp. 91–110, 2004.

[43] W. Liu, D. Anguelov, D. Erhan, C. Szegedy, S. Reed, C.-Y. Fu, and A.-C. Berg, "SSD: Single shot multibox detector," in *Proc. Eur. Conf. Comput. Vis.*, Amsterdam, Netherlands, Oct. 2016, pp. 21–37.

[44] X. Fu, Y. Liao, D. Zeng, Y. Huang, X.-P. Zhang, and X. Ding, "A probabilistic method for image enhancement with simultaneous illumination and reflectance estimation," *IEEE Trans. Image Process.*, vol. 24, no. 12, pp. 4965–4977, 2015.

[45] J. Canny, "A computational approach to edge detection," *IEEE Trans. Pattern Anal. Mach. Intell.*, vol. 6, pp. 679–698, 1986.

[46] C. Harris and M. Stephens, "A combined corner and edge detector," in *Proc. Alvey Vis. Conf.*, Manchester, UK, pp. 147–151, 1988.

[47] M. Yang and A. Sowmya, "An underwater color image quality evaluation metric," *IEEE Trans. Image Process.*, vol. 24, no. 12, pp. 6062–6071, 2015.

[48] K. Panetta, C. Gao, and S. Agaian, "Human-visual-system-inspired underwater image quality measures," *IEEE J. Ocean. Eng.*, vol. 41, no. 3, pp. 541–51, 2015.

[49] A. Galdran, D. Pardo, A. Picon, and A. Alvarez-Gila, "Automatic red-channel underwater image restoration," *J. Vis. Commun. Image Represent.*, vol. 26, pp. 132–145, 2015.

SUPPLEMENTAL MATERIALS

A. Network Architecture

Let $\text{Conv}(i, o, k, s, p)$ be a convolution layer with i, o, k, s, p as the input channel, output channel, kernel size, stride, and padding, respectively; $\text{ConvT}(i, o, k, s, p, op)$ represents a deconvolution layer with op as the output padding; $\text{RefPad}(pt, pb, pl, pr)$ is the reflection padding operation; $\text{Drop}(prob)$ is the dropout layer with $prob$ as the probability; BN denotes the batch normalization; and ReLU, Tanh, LeakyReLU are activation functions.

1) Residual Block:

$$\begin{aligned} & \text{RefPad}(1, 1, 1, 1) \\ & \rightarrow \text{Conv}(256, 256, 3, 1, 0) \rightarrow \text{BN} \rightarrow \text{ReLU} \\ & \rightarrow \text{Drop}(0.5) \rightarrow \text{RefPad}(1, 1, 1, 1) \\ & \rightarrow \text{Conv}(256, 256, 3, 1, 0) \rightarrow \text{BN} \end{aligned}$$

2) Generative Model:

$$\begin{aligned} & \text{RefPad}(3, 3, 3, 3) \\ & \rightarrow \text{Conv}(3, 64, 7, 1, 0) \rightarrow \text{BN} \rightarrow \text{ReLU} \\ & \rightarrow \text{Conv}(64, 128, 3, 2, 1) \rightarrow \text{BN} \rightarrow \text{ReLU} \\ & \rightarrow \text{Conv}(128, 256, 3, 2, 1) \rightarrow \text{BN} \rightarrow \text{ReLU} \\ & \rightarrow 9 \times \text{Residual Blocks} \\ & \rightarrow \text{ConvT}(256, 128, 3, 2, 1, 1) \rightarrow \text{BN} \rightarrow \text{ReLU} \\ & \rightarrow \text{ConvT}(128, 64, 3, 2, 1, 1) \rightarrow \text{BN} \rightarrow \text{ReLU} \\ & \rightarrow \text{RefPad}(3, 3, 3, 3) \rightarrow \text{Conv}(64, 3, 7, 1, 0) \rightarrow \text{Tanh} \end{aligned}$$

3) Adversarial Branch (AB):

$$\begin{aligned} & \text{Conv}(64, 128, 4, 2, 1) \rightarrow \text{BN} \rightarrow \text{LeakyReLU}(0.2) \\ & \rightarrow \text{Conv}(128, 256, 4, 2, 1) \rightarrow \text{BN} \rightarrow \text{LeakyReLU}(0.2) \\ & \rightarrow \text{Conv}(256, 512, 4, 2, 1) \rightarrow \text{BN} \rightarrow \text{LeakyReLU}(0.2) \\ & \rightarrow \text{Conv}(512, 512, 4, 1, 1) \rightarrow \text{BN} \rightarrow \text{LeakyReLU}(0.2) \\ & \rightarrow \text{Conv}(512, 1, 4, 1, 1) \end{aligned}$$

4) Underwater Branch (UB):

$$\begin{aligned} & \text{Conv}(64, 128, 4, 2, 1) \rightarrow \text{BN} \rightarrow \text{LeakyReLU}(0.2) \\ & \rightarrow \text{Conv}(128, 256, 4, 2, 1) \rightarrow \text{BN} \rightarrow \text{LeakyReLU}(0.2) \\ & \rightarrow \text{Conv}(256, 512, 4, 2, 1) \rightarrow \text{BN} \rightarrow \text{LeakyReLU}(0.2) \\ & \rightarrow \text{Conv}(512, 512, 4, 2, 1) \rightarrow \text{BN} \rightarrow \text{LeakyReLU}(0.2) \\ & \rightarrow \text{Conv}(512, 512, 4, 1, 1) \rightarrow \text{BN} \rightarrow \text{LeakyReLU}(0.2) \\ & \rightarrow \text{Conv}(512, 1, 4, 1, 1) \end{aligned}$$

5) Discriminative Model:

$$\text{Conv}(64, 128, 4, 2, 1) \rightarrow \text{LeakyReLU}(0.2) \left\{ \begin{array}{l} \rightarrow \text{UB} \\ \rightarrow \text{AB} \end{array} \right.$$

B. Computation of Receptive Field

The receptive field (RF) size of $(C - 1)$ -layer can be calculated from the up layer with $\text{size}_{rf}^{C-1} = (\text{size}_{rf}^C - 1) * s + k$. For bounding box position, the RF coordinates can be calculated. That is, $(x_{min}^{C-1}, x_{max}^{C-1}, y_{min}^{C-1}, y_{max}^{C-1})$ in layer $C - 1$ are given as follows:

$$\left\{ \begin{array}{l} x_{min}^{C-1} = (x^C) \times s + 1 - p \\ x_{max}^{C-1} = (x^C) \times s - p + k \\ y_{min}^{C-1} = (y^C) \times s + 1 - p \\ y_{max}^{C-1} = (y^C) \times s - p + k \end{array} \right.$$

C. Discrimination Details

There are several improvements for discriminator in this paper, but the generator received more attention in the experiments. To unveil more details about the discriminator, the patch underwater index (PU) given by D will be presented numerically at first. In addition, typical processing results are presented in larger scale. In the meantime, the corresponding adversarial maps (Ad-map) and underwater index maps (U-map) will be visualized. Note that the sizes of underwater map and adversarial map are $6 \times 6, 14 \times 14$, respectively. For visual convenience, they are all presented in the same size as the image, which unveil the effectiveness of the improvements for the discriminator in this paper.

1) Patch Underwater Index for Fig. 3(b):

$$PU_{FRS} =$$

$$\left(\begin{array}{ccccccc} 0.9619 & 0.8644 & 0.7543 & 0.7331 & 0.7372 & 0.7386 \\ 0.7989 & 0.7415 & 0.6481 & 0.6349 & 0.6233 & 0.6590 \\ 0.7303 & 0.6845 & 0.5958 & 0.5693 & 0.5400 & 0.5658 \\ 0.6569 & 0.6319 & 0.5612 & 0.5459 & 0.5275 & 0.5497 \\ 0.6599 & 0.6018 & 0.5104 & 0.4779 & 0.5045 & 0.5301 \\ 0.6998 & 0.6179 & 0.5011 & 0.4796 & 0.4861 & 0.5080 \end{array} \right)$$

$$PU_{GAN-RS} =$$

$$\left(\begin{array}{ccccccc} 0.3572 & 0.3363 & 0.3025 & 0.2975 & 0.3266 & 0.3253 \\ 0.2954 & 0.2804 & 0.2610 & 0.2452 & 0.2646 & 0.2668 \\ 0.2975 & 0.2962 & 0.2816 & 0.2460 & 0.2322 & 0.2559 \\ 0.2848 & 0.2888 & 0.2603 & 0.2231 & 0.2112 & 0.2230 \\ 0.2700 & 0.2681 & 0.2547 & 0.2277 & 0.2055 & 0.2234 \\ 0.2746 & 0.2640 & 0.2412 & 0.2155 & 0.1914 & 0.1924 \end{array} \right)$$

2) Patch Underwater Index for Fig. 4(a):

$$PU_{FRS} =$$

$$\left(\begin{array}{ccccccc} 0.6640 & 0.5746 & 0.5640 & 0.5356 & 0.5485 & 0.5204 \\ 0.6478 & 0.5703 & 0.5515 & 0.5133 & 0.5360 & 0.5329 \\ 0.6639 & 0.5809 & 0.5547 & 0.5058 & 0.5216 & 0.5216 \\ 0.6447 & 0.5486 & 0.5143 & 0.4496 & 0.4516 & 0.4593 \\ 0.6183 & 0.5186 & 0.4844 & 0.4463 & 0.4312 & 0.4341 \\ 0.5972 & 0.5046 & 0.4864 & 0.4552 & 0.4340 & 0.4479 \end{array} \right)$$

$$PU_{GAN-RS} =$$

$$\left(\begin{array}{ccccccc} 0.2932 & 0.2509 & 0.2351 & 0.2222 & 0.2274 & 0.2297 \\ 0.2941 & 0.2540 & 0.2402 & 0.2134 & 0.2262 & 0.2258 \\ 0.3080 & 0.2703 & 0.2479 & 0.2192 & 0.2164 & 0.2189 \\ 0.2942 & 0.2512 & 0.2310 & 0.1903 & 0.1887 & 0.1861 \\ 0.2853 & 0.2364 & 0.2124 & 0.1763 & 0.1839 & 0.1825 \\ 0.2932 & 0.2388 & 0.2031 & 0.1715 & 0.1587 & 0.1633 \end{array} \right)$$

3) Visualization of Underwater Map and Adversarial Map:

The adversarial branch is able to roughly distinguish the real and the generated, but the content and structure in an image have been preserved. Meanwhile, the underwater branch has capacity of reducing PU . Furthermore, G has found a compromise between the two branches, and generated better images.

